nature geoscience

SUPPLEMENTARY INFORMATION

DOI: 10.1038/NGEO2166

Changbaishan volcanism in northeast China linked to subduction-induced mantle upwelling

Youcai Tang, Masayuki Obayashi, Fenglin Niu, Stephen P. Grand, Yongshun John Chen, Hitoshi Kawakatsu, Satoru Tanaka, Jieyuan Ning, James F Ni

S1. *S*-wave tomography

We used the finite-frequency tomography method[33,34] to invert for S-wave velocity structure in the mantle beneath Northeast China. The method employs Born-Fréchet kernels to account for effects of off-raypath structures on traveltime data. The data used in the inversion are differential travel times between station pairs. Distance between station pairs are chosen to be ≤ 200 km to ensure the measured differential times reflect velocity perturbations beneath the array. At such a separation, since raypaths from a teleseismic event to the two stations are nearly identical outside the array, any velocity anomalies outside the study area are expected to have minimal effects on the differential travel times between the two stations. The travel times were first corrected for surface topography and crustal structure derived from receiver function data[35] before the inversion. The differential travel times between two stations were measured based on cross correlation of S, SKS and SKKS arrivals recorded at epicentral distance between 30° and 180° (Fig. S1). The total number of earthquakes used in the measurement is 99, 27 and 17 for the S, SKS and SKKS arrivals, respectively. To account for frequency effects, we further filtered the data to three frequency bands: 0.02-0.05 Hz, 0.05-0.1 Hz, and 0.1-0.5 Hz, and measured differential travel times separately for data in each band. Table S1 shows the total number of differential travel-time measurements for each frequency band.

Table S1. Number of differential traveltime measurements.

	0.02-0.05 Hz	0.05-0.1 Hz	0.1-0.5 Hz
S	7625	9857	6007
SKS	238	1612	1578
SKKS	237	233	777

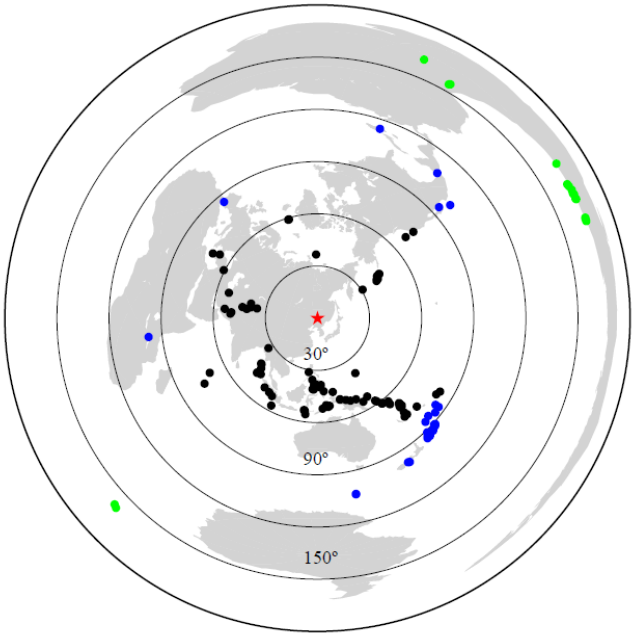

Figure S1. Distribution of the 143 earthquakes used in the *S*-wave tomography. The red star indicates the center of the seismic array. Black, blue and green dots denote earthquakes that were used to measure travel times of *S*, *SKS* and *SKKS* phases, respectively.

We divided the study volume (36°N to 53°N, 113°E to136°E, 0 to 1400 km deep) into 0.2º by 0.2º by 20 km grid points. The initial model was scaled from the global P-wave model (GAP_P2)[36] with a scaling factor of 1.75. The linear system of equations for S-wave velocity perturbations is solved with the iterative LSQR[37] algorithm by imposing a second-order smoothness constraint and damping to suppress artificial and large fluctuations of the solution. The weights of smoothing and damping were selected using the L-curve criterion[38].

S2. Resolution tests

We performed a checkerboard test to show the resolution of the differential travel-time data on S-wave structure beneath the array. To do so, we first created checkerboard anomalies with alternating 3% faster and slower velocity anomalies. The size of each block is roughly 200 km by 200 km. We then generated a synthetic travel-time dataset using earthquakes and stations identical to the observed differential travel-time data. Random noise ranging from -0.2 s to 0.2 s was added to the synthetic data. Fig. S2 shows the results of the recovered checkerboards at four different depths. The checkerboard model was well reconstructed in both the alternating pattern and amplitude above a depth of 500 km. The recovered amplitude

of the checkerboard anomalies decreases steadily with increasing depth though. For structures below 500 km depth, significant smearing occurs at the edge of the study area and the recovered velocity perturbations are only half of the input values.

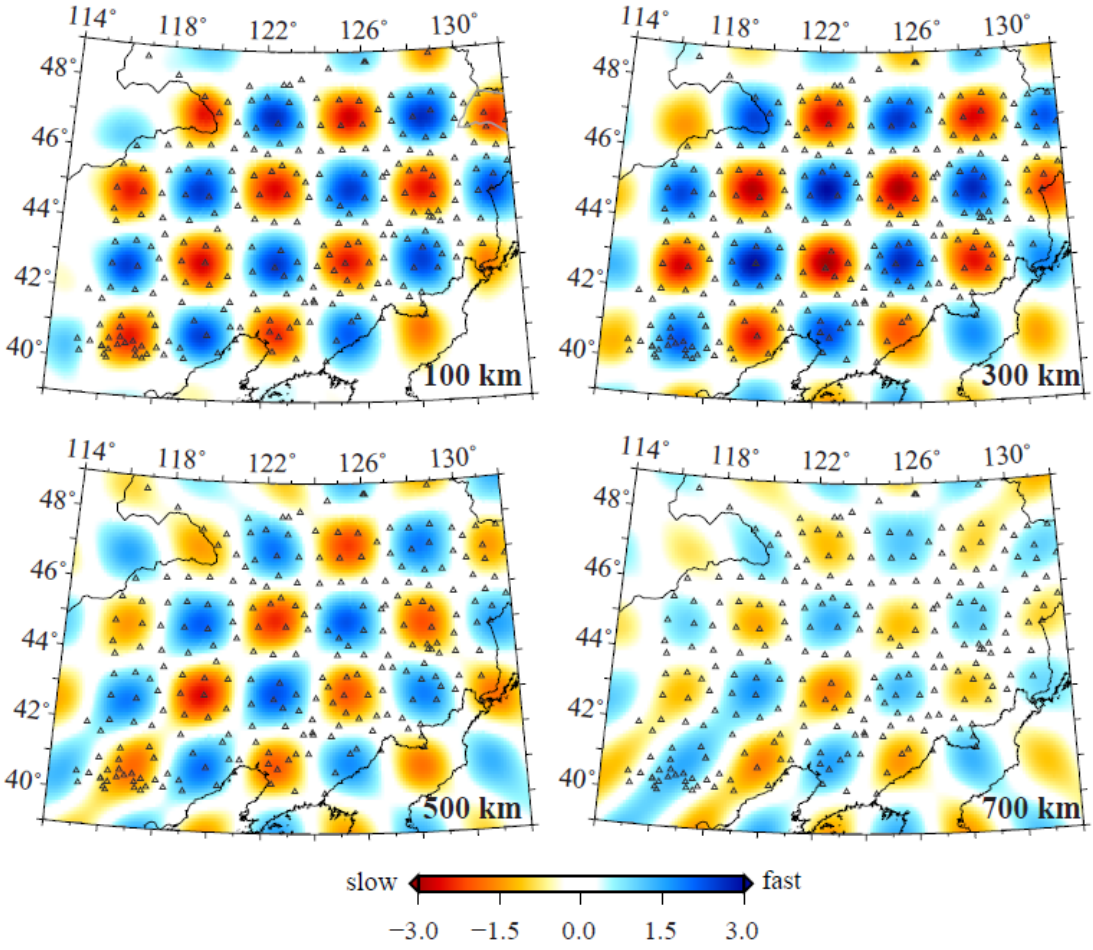

at depths of 100 km, 300 km, 500 km, and 700 km obtained from the checkerboard test. The test indicates that the *S*-wave differential travel-time data has good resolution at length scales of ~200 km in the study region. Note that the amplitude of the velocity anomalies in the recovered model decays steadily with depth.

We also performed another test to see whether the slow cylindrical anomaly in the transition zone shown in Fig. 3a is a robust structure required by the travel-time data. To do so, we first built a test velocity model by removing the slow cylindrical anomaly in the NECESS S-wave model (TM1, Fig. S3a). We then generated synthetic travel times by using the TM1 model and earthquake-station pairs similar to the observed data. These synthetic travel-time data were first inverted to see whether there is artificial structure put inside the green circle. Figure S3b shows the resulting model, which is essentially similar to the input

model. There is no slow anomaly inside the green circle in the recovered model. To further demonstrate that the slow anomaly inside the green circle is required by the observed travel-time data, we subtracted the TM1 synthetic data from the corresponding observations to generate a travel-time residual dataset. In order to find structures responsible for the travel-time residuals, we simply inverted the residual data for an incremental S-wave velocity model using model TN1 as the starting model. Figure S3c shows the final model, which has a strong slow velocity anomaly inside the green circle, suggesting that this slow velocity anomaly is required by the travel-time data. Based on this test, we conclude that the slow anomaly inside the green circle is not an artifact of the inversion.

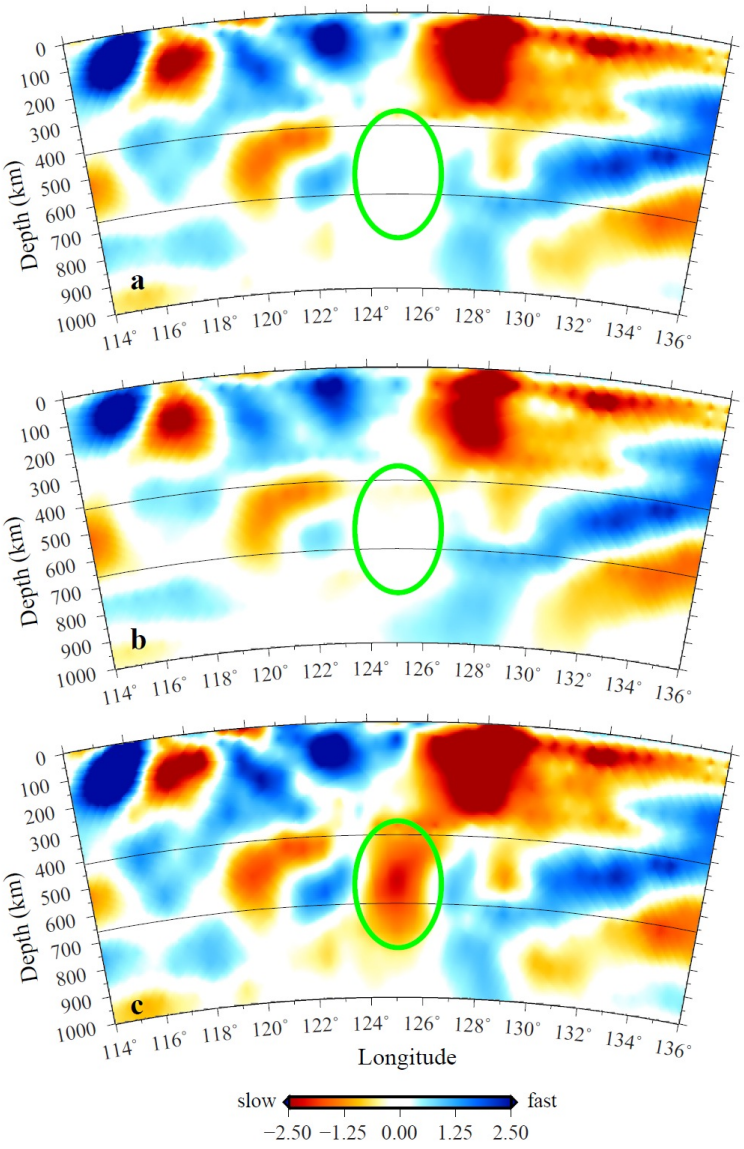

Figure S3. Robustness test of the transition zone upwelling. (**a**) The input TM1 model modified from the NECESS *S*-wave model. (**b**) Recovered model inverted with TM1 synthetic data. (**c**) The model derived by inverting residual data and using the model in (**b**) as a starting model. Note that the distinct low-velocity anomaly inside the green circle is a robust structure required by the data.

S3. *P*-wave tomography

The P-wave model was obtained by inverting a mixed travel-time dataset, which consists of ~11.5 million first arrival times from the ISC Bulletins, ~60,000 P arrivals manually picked from seismic networks deployed in the central and western Pacific regions, ~15,000 PP-P differential travel times measured with a waveform correlation based technique, and ~21,000 travel times measured from the NECESSArray data. The first three types of data were used to construct the global model GAP_P2[36] published a few years ago. Therefore the NECESS P-wave model can be considered as the updated version of the whole mantle model of GAP_P2. The ~21,000 NECESSArray travel times are first arrival picks and relative travel times of P-wave between station pairs from ~100 events. The relative travel times are measured by a cross-correlation based method at nine frequency bands whose center periods are 30, 21.2, 15, 10.6, 7.5, 5.3, 3.7, 2.7 and 1.9, respectively. Finite frequency effects were taken into account by using the Born approximation in computing the traveltime kernels. The mantle was discretized into blocks with variable sizes that depend on the sampling density of the travel-time data. The largest and smallest blocks are 5.0°×5.0° and 0.625°×0.625° in lateral size, respectively. The study region was parameterized with the smallest blocks.

S4. Receiver functions

The receiver functions were computed from the data projected into P- and SV-components[39-41]. We employed the 'water-level' deconvolution technique[42] to generate receiver functions. We used a 100 s time window (5 s and 95 s before and after the P wave) to compute the source spectrum of each earthquake. We further screened receiver functions with various methods[43] to eliminate noisy data. The total number of receiver functions used in the CCP imaging is 45505.

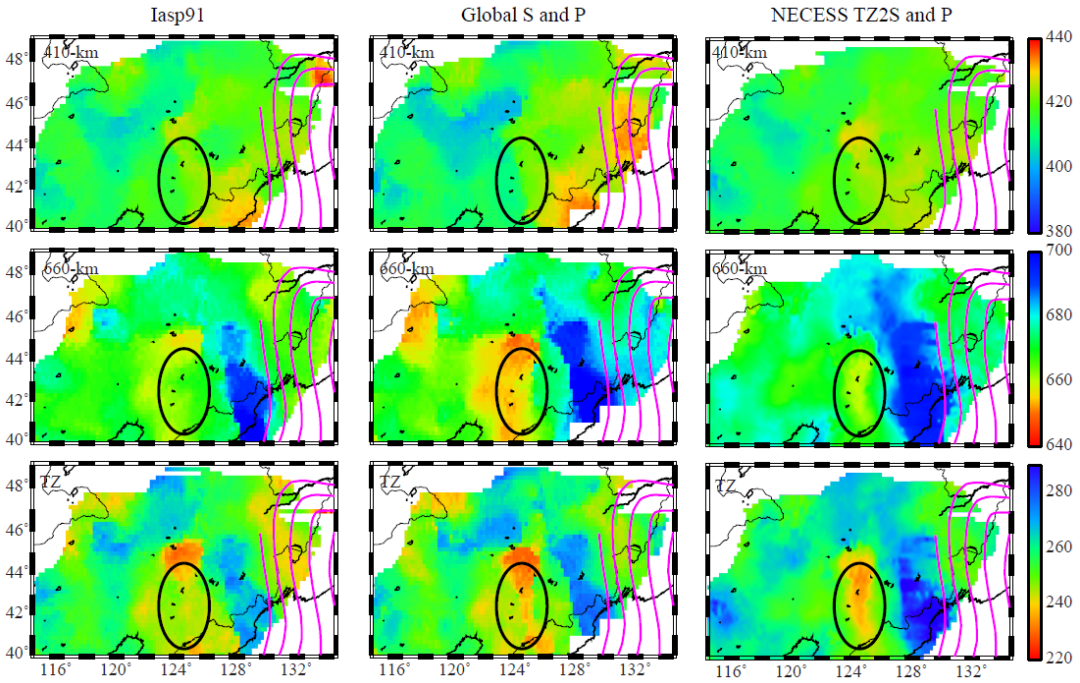

Figure S4. Maps showing the depth to the 410-km (top), 660-km (middle) discontinuities, and thickness of the transition zone (bottom). The left, middle and right panels are computed from the iasp91, 3D global and NECESS velocity models. The black circle denotes the location of the slow anomaly shown in Fig. 2.

We applied the CCP stacking technique to the receiver-function data to image the P-to-S (Ps) conversion events and their lateral variations beneath the array[41,44,45]. For an assumed conversion depth, *d*, we first computed the relative arrival time of the converted phase Ps with respect to the direct arrival by ray tracing the two phases using the 1D iasp91 velocity model[46]. We also kept the geographic location of the conversion points and gathered the receiver functions that share the same conversion points. We divided the study area (40°N to 49°N, 115°E to 135°E) into meshed grids of 0.1º by 0.1º, and used a circular cap with a radius of 1 degree for gathering the receiver functions. The total number of the caps is 18291 (91×201), and there are significant overlaps among the caps. This serves as a low-pass filter that smoothens the topographic relief on the two discontinuities with a corner wavelength roughly equivalent to the size of the caps, i.e., ~200 km. We then linearly stacked all the receiver functions within a 0.2 s window centered on the arrival time of Ps. The depths to the 410-km and 660-km discontinuities, as well as the transition zone thickness are shown in the left column of Fig. S4.

To better image the absolute depths of the two discontinuities, we further used observed Moho Ps arrival times to correct for the crustal effect, which appears to be in the range of +3 to -3 km. The mantle corrections on the relative Ps traveltime were computed with two sets of P- and S-wave models. The first set is the whole mantle P from Fukao et al. (2001)[47] derived from ISC traveltime data, and the S-wave velocity model from Grand (2002)[48]. The second pair is the NECESS P and S with doubled anomaly amplitude in transition zone (TZ2S model). In each case, we computed 3D travel-time tables for each receiver function, conducted the CCP stacking, and manually picked the depths of the two discontinuities. The results using the global and NECESS models are shown in the middle and right panels of Fig. S4, respectively.

S5. Waveform modeling

We used the spectral-element method (SPECFEM3D)[12] to conduct 3D forward modeling of S waveform data from one intermediate-depth earthquake occurring in the Banda Sea on July 16, 2011 (PDE: 2011-07-16, 17:06:39.61, -7.100°, 127.576°, 254.7 km, 5.9 Mw) and one deep focus earthquake beneath Mindanao, Philippines on October 4, 2009 (PDE: 2009-10-04, 10:58:00.17, 6.740°, 123.378°, 620.0 km, 6.6 Mw) (Fig. 4). We applied a Butterworth filter to the SH displacement waveforms. The corner frequencies of the bandpass filter are 0.02 and 0.2 Hz. We first built an isotropic 3D mantle model by superposing the S-wave velocity perturbations of the NECESS S model on the 1D PREM model[49]. The 3D mantle model is then combined with the crust model from receiver functions and ETOPO5 (the National Oceanic and Atmospheric Administration, 1998) to construct a whole earth 3D model. For comparison, we also built another 3D model using the NECESS TZ2S model. In both models, we set the S-wave velocity perturbation to zero outside the study region. Perturbations in P-wave velocity and density are computed from the S-wave velocity using a scaling factor of 0.6 and 0.4, respectively. Fig. S5 and Fig. S6 show the waveform comparison for the two earthquakes (Fig. 4). The synthetic waveforms using model TZ2S (Fig. S5a and Fig. S6a) fit the data better than using NECESS S model (Fig. S5b and Fig. S6b).

The synthetic waveforms are computed using 648 cores on the Stampede Linux Cluster at the Texas Advanced Computing Center (TACC). The average grid spacing is 5.79 km, corresponding to a dominant period of 3.3 s.

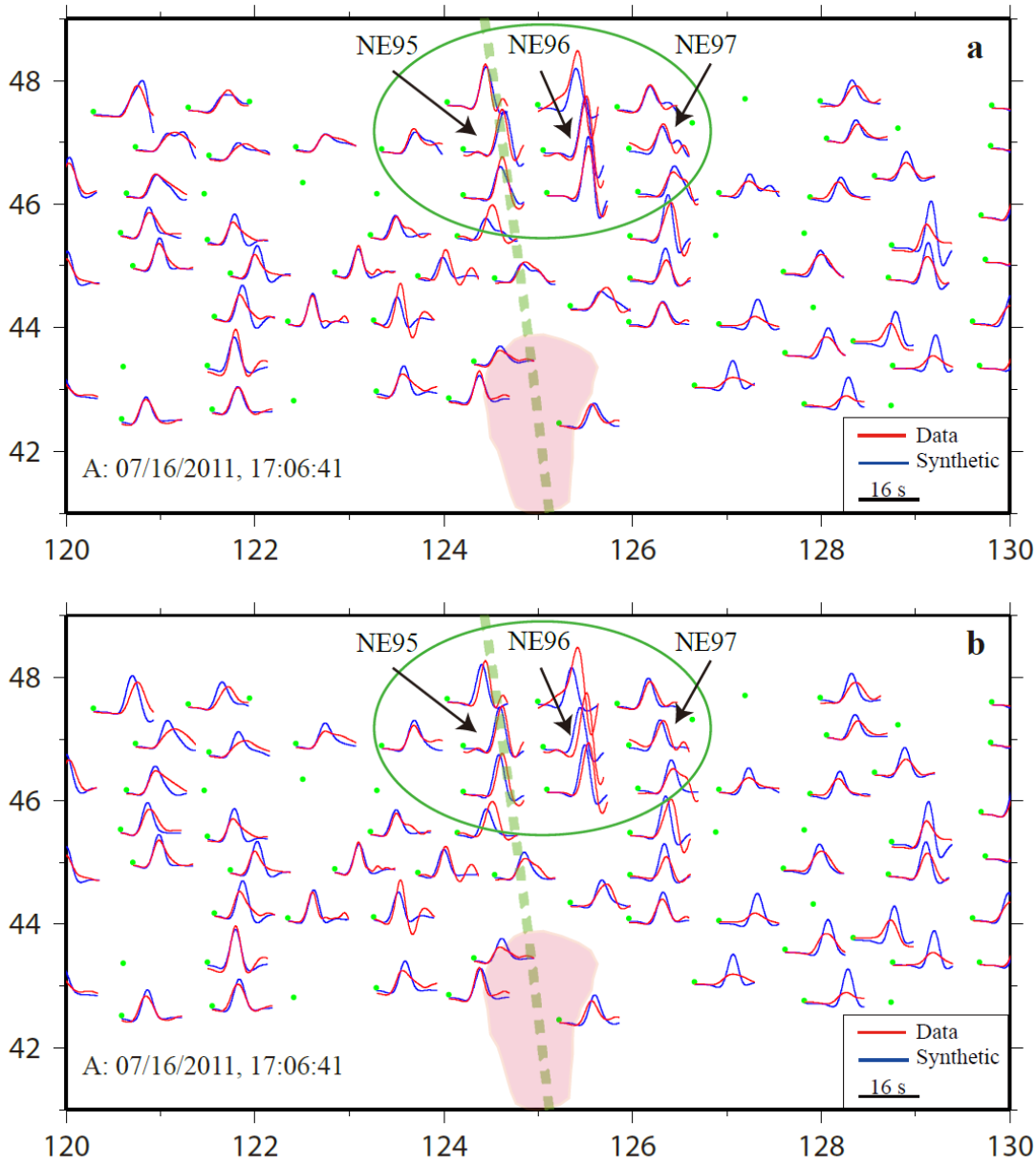

Figure S5. 3D waveform modeling. (a) and (b) show *SH* waveform comparisons for earthquake A (Fig. 4) using velocity models TZ2S and NECESS S, respectively. The green dashed lines correspond to the AA' profile (Fig. 4). The pink region denotes the geographic location of the strong slow anomaly in the transition zone. Green ellipses mark the stations that have the biggest differences between the synthetics using different models.

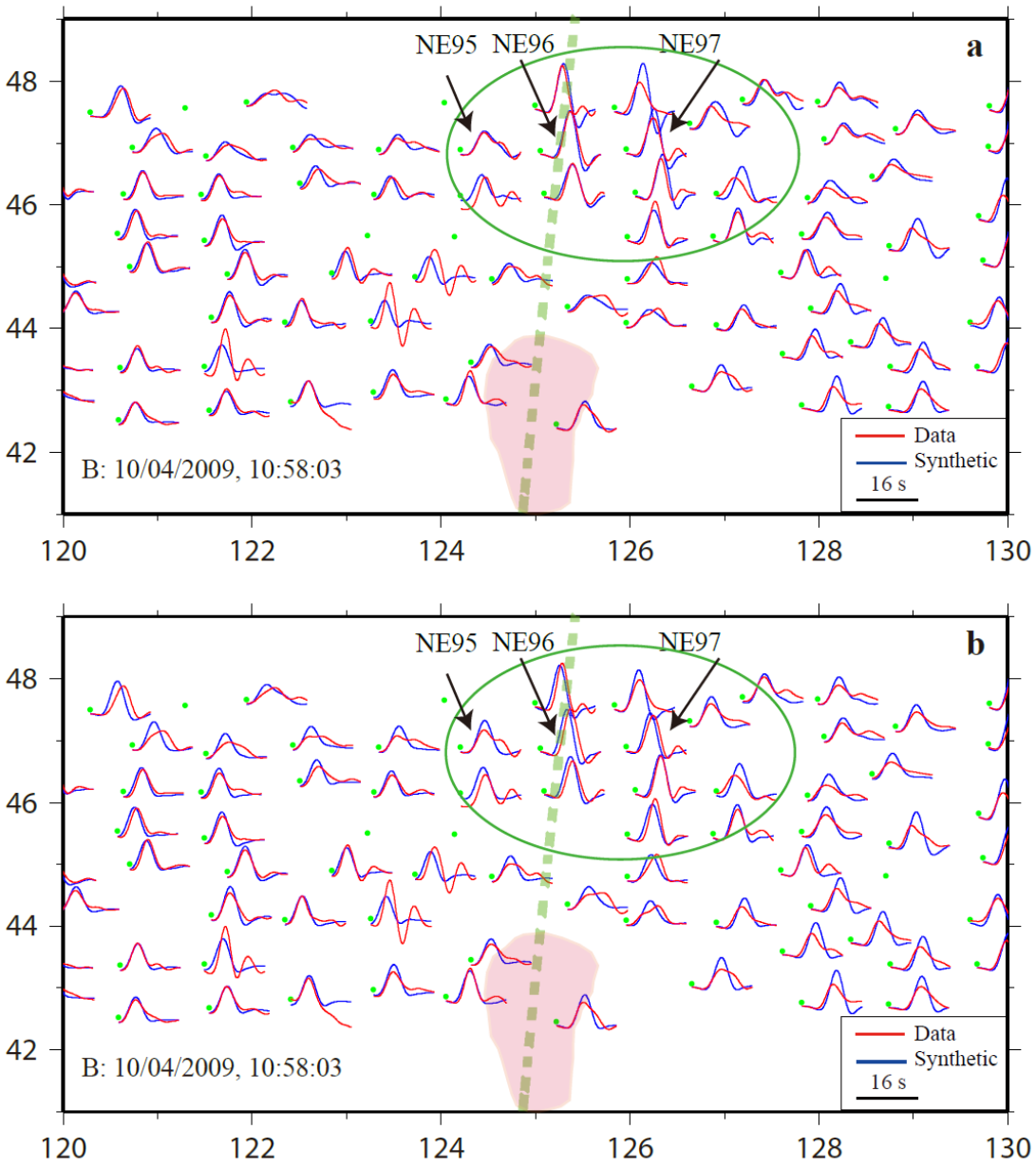

Figure S6. 3D waveform modeling. (a) and (b) show *SH* waveform comparisons for earthquake B (Fig. 4) using velocity models TZ2S and NECESS S, respectively. The green dashed lines correspond to the BB' profile (Fig. 4). The pink region denotes the geographic location of the strong slow anomaly in the transition zone. Green ellipses mark the stations that have the biggest differences between the synthetics using different models.

33. Liang, X., Shen, Y., Chen, Y.J., & Ren, Y. Crustal and mantle velocity models of southern Tibet from finite frequency tomography. *J. Geophys. Res.* **116**, B02408, doi:10.1029/2009JB007159 (2011).

34. Hung, S.-H., Shen, Y., & Chiao, L.-Y. Imaging seismic velocity structure beneath the Iceland hot spot: A finite frequency approach. *J. Geophys. Res.* **109**, B02408, doi:10.1029/2009JB007159 (2004).

35. Liu, Z., et al. Receiver function images of the mantle transition zone beneath NE China: new constraints on intraplate volcanism, deep subduction and their potential link. Abstract **DI11A-2379**, *presented at 2012 Fall meeting, AGU*, San Francisco, Calif., 3-7 Dec. (2012).

36. Obayashi, M., Yoshimitsu, J., & Fukao, Y. Tearing of Stagnant Slab. *Science* **324**, 1173-1175 (2009).

37. Paige, C.C., & Saunders, M.A. LSQR: An Algorithm for Sparse Linear Equations and Sparse Least Squares. ACM Transastions on Mathematical Software *Trans. Math. Software*, **8**, 43–71, doi:10.1145/355984.355989 (1982).

38. Hansen, P C. Analysis of discrete ill-posed problems by means of the L-curve. *SIAM review* **34**, 561-580 (1992).

39. Vinnik, L.P. Detection of waves converted from P to SV in the mantle. *Phys. Earth Planet. Inter.* **15**, 39-45 (1977).

40. Niu, F., & Kawakatsu, H. Determination of the absolute depths of the mantle transition zone discontinuities beneath China: Effect of stagnant slabs on transition zone discontinuities. *Earth Planets Space* **50**, 965-976 (1998).

41. Niu, F. L., Levander, A., Ham, S., & Obayashi, M. Mapping the subducting Pacific slab beneath southwest Japan with Hi-net receiver functions. *Earth Planet. Sci. Lett.* **239**, 9-17 (2005).

42. Clayton, R.W., & Wiggins, R.A. Source shape estimation and deconvolution of teleseismic bodywaves. *Geophys. J. R. Astr. Soc.* **47**, 151-177 (1976).

43. Chen, Y. et al. Crustal structure beneath China from receiver function analysis. *J. Geophys. Res.* **115**, B03307, doi:10.1029/2009JB006386 (2010).

44. Dueker, K.G., & Sheehan, A.F. Mantle discontinuity structure from midpoint stacks of converted P to S waves across the Yellowstone hotspot track. *J. Geophys. Res.* **102**, 8313-8327 (1997).

45. Gilbert, H.J., Sheehan, A.F., Dueker, K.G., & Molnar, P. Receiver functions in the western United States, with implications for upper mantle structure and dynamics. *J. Geophys. Res*. **108**, 2229, doi:10.1029/2001JB001194 (2003).

46. Kennett, B.L.N., & Engdahl, E.R. Traveltimes for global earthquake location and phase identification. *Geophys. J. Int.* **105**, 429-465 (1991).

47. Fukao, Y., Widiyantoro, S., & Obayashi, M. Stagnant slabs in the upper and lower mantle transition region. *Rev. Geophys.* **39**, 291-323 (2001).

48. Grand, S.P. Mantle shear-wave tomography and the fate of subducted slabs. *Philos. T. Roy. Soc. A*. **360**, 2475-2491 (2002).

49. Dziewonski, A. M., Anderson, D. L. Preliminary reference Earth model. *Phys. Earth Planet. Inter*. **25**, 297-356 (1981).